

Higher order Fano graphene metamaterials for nanoscale optical sensing

Xiangdong Guo,^{abcd} Hai Hu,^{ac} Xing Zhu,^{abd} Xiaoxia Yang^{*a} and Qing Dai ^{*ac}

* Corresponding authors

^a China CAS Center for Excellence in Nanoscience, National Center for Nanoscience and Technology, Beijing 100190, P. R. China

E-mail: daiq@nanoctr.cn, yangxx@nanoctr.cn

Tel: +86-010-82545720

^b Academy for Advanced Interdisciplinary Studies, Peking University, Beijing 100871, P. R. China

^c University of Chinese Academy of Sciences, Beijing 100049, P. R. China

^d State Key Lab for Mesoscopic Physics, School of Physics, Peking University, Beijing 100871, P. R. China

Abstract:

Plasmonic Fano metamaterials provide a unique platform for optical sensing applications due to their sharp spectral response and the ability to confine light to nanoscale regions that make them a strong prospect for refractive-index sensing. Higher order Fano resonance modes in noble metal plasmonic structures can further improve the sensitivity, but their applications are heavily limited by crosstalk between different modes due to the large damping rates and broadband spectral responses of the metal plasmon modes. Here, we create pure higher order Fano modes by designing asymmetric metamaterials comprised of a split-ring resonator and disk with a low-loss graphene plasmon. These higher order modes are highly sensitive to the nanoscale analyte (8 nm thick) both in refractive-index and in infrared vibrational fingerprint sensing, as demonstrated by the numerical calculation. The frequency sensitivity and figure-of-merit of the hexacontatetrapolar mode can reach 289 cm^{-1} per RIU and 29, respectively, and it can probe the weak infrared vibrational modes of the analyte with

30 more than 400 times enhancement. The enhanced sensitivity and tunability of higher
31 order Fano graphene metamaterials promise a high-performance nanoscale optical
32 sensor.
33

34 **Introduction**

35 Fano resonance with spectrally narrow optical responses and high local field
36 enhancement has been demonstrated in plasmonic metamaterials,¹⁻³ which has allowed
37 it to emerge as a powerful photonic platform for sensing applications.⁴⁻⁹ Plasmonic
38 Fano structures can detect small amounts of molecules by measuring frequency shifts
39 of the narrow optical response induced by a refractive index change of the local
40 environment.^{1,5,6,9} Based on this application, many noble metal Fano structures have
41 been designed, such as the ring/disk cavity,^{4,10,11} “XI” shape structure¹² and many
42 others. Plasmonic Fano resonances are the coupling of the bright plasmon modes (broad)
43 and dark plasmon modes (narrow). The dipolar (D) plasmon is often the bright mode,
44 which can be directly excited by the normally incident light. In contrast, the higher
45 order (quadrupolar (Q), octupolar (O), hexadecapolar (H), triakontadipolar (T), *etc.*)
46 plasmons are usually the dark modes, which are hard to be optically excited.

47 In order to enhance the sensitivity of the refractive-index sensor, the plasmon resonance
48 should satisfy basic characteristics: a high spectral shift $\delta\lambda/\delta n$ (refractive index) and a
49 narrow line width.¹² The higher order plasmons have the sharper peaks with higher
50 quality factors.¹³ In Fano structures, the higher order modes would be exhibited and the
51 same refractive index change could induce larger frequency shifts with mode order
52 increases. Thus the higher order Fano resonances have greater sensitivity in refractive-
53 index sensing.^{6,9,14} However, in noble metal systems, crosstalk can potentially exist in
54 many adjacent higher order modes,^{9,14} which originates from the large plasmonic
55 damping rates and broad-band spectral responses of the bright mode. For example,
56 different higher order Fano modes interact with each other in the gold ring/disk cavity,
57 where the disk's dipolar plasmon acts as a bright mode and the ring's multipolar
58 plasmons act as dark modes. To overcome this problem and to realize high quality,
59 higher order Fano resonance for ultra-sensitive refractive index sensing, graphene
60 plasmons with low damping rates¹⁵⁻¹⁷ and high field confinement could be used.

61 In addition to sensitive refractive-index sensing, graphene plasmons in the infrared
62 frequency range can also be used for surface-enhanced infrared absorption (SEIRA).¹⁸⁻
63 ²⁰ SEIRA, which can directly provide chemical information about analytes by

64 characterizing their molecular fingerprints, is complementary to refractive index
65 sensors.²¹ The high local field enhancement in plasmonic Fano structures means the
66 high sensitivity of SEIRA. Moreover, the Fano resonance creates two resonant
67 absorption peaks with wide spectral ranges, which can enhance multiple vibration
68 signals of molecules at a given time. Thus, it provides a platform for multispectral
69 biosensing.²

70 In this manuscript, the low damping graphene plasmon is used to generate separate
71 higher order Fano modes for enhanced refraction-index sensing and SEIRA. We adapt
72 a commonly used hybrid structure of a split-ring resonator (SRR) and disk,²²⁻²⁴ where
73 the higher order plasmon resonance excited in the SRR act as a dark mode and the
74 dipolar plasmon resonance of the graphene disk acts as a bright mode. Each higher
75 order Fano resonance, *i.e.* H, T, and hexacontatetrapolar (HC) Fano, can be realized by
76 choosing an appropriate size of the graphene disk. As the mode order increases, its
77 sensitivity to the refractive index change increases. The sensitivity of the HC Fano
78 mode reaches 289 cm^{-1} per RIU, corresponding to a FOM of 29 for the refractive-index
79 sensor. Moreover, the highly confined electromagnetic field of these higher order Fano
80 resonances can also be used to enhance the molecular vibrational modes.

81 **Results and discussion**

82 **Structural design and physical mechanism**

83 A schematic of the graphene metamaterials for the higher order Fano resonance is
84 shown in Fig. 1. They are comprised of a graphene disk positioned inside a graphene
85 SRR in a unit cell. The unit cells are arranged in a square lattice. The 300 nm CaF_2 film
86 is chosen as a substrate over commonly used substrates like SiO_2 and $h\text{-BN}$,^{16,25} since
87 CaF_2 is transparent and has no phonon that can interact with the graphene plasmon in
88 the infrared spectral region.^{18,26,27} The proposed Fano resonance is excited by a plane
89 wave propagating in the z -direction with an electric field polarized in the x -direction.

90 The higher order Fano resonances of the graphene metamaterials are simulated
91 employing the finite element method (FEM). Graphene is modeled as a material with
92 finite thickness and equivalent relative permittivity, which is thickness dependent. The
93 equivalent relative permittivity is derived from the surface conductivity. It is calculated

94 by $\varepsilon_g = i\sigma/\varepsilon_0\omega t_g$,²⁸ where ε_0 is the permittivity of free space and the graphene layer
 95 thickness is $t_g = 1$ nm, at which the calculations reach proper convergence. Thus the
 96 graphene layer is treated as the transition boundary condition. The permittivity of
 97 CaF₂ is obtained from the handbook.²⁹ To balance the 3D FEM calculated amount and
 98 the mesh quality, the smallest mesh size of graphene is 0.5 nm and the mesh size
 99 gradually increases outside the graphene layer.

100 To calculate the surface conductivity of graphene, σ , the Kubo formula^{30–33} is used,
 101 which consists of interband and intraband transitions. At room temperature ($T = 300$ K),
 102 which satisfies the requirement of $K_B T \ll E_f$, the expression is approximated as:

$$\sigma = \frac{ie^2 E_f}{\pi \hbar^2 (\omega + i\tau^{-1})} + \frac{ie^2}{4\pi \hbar} \ln \left[\frac{2|E_f| - \hbar(\omega + i\tau^{-1})}{2|E_f| + \hbar(\omega + i\tau^{-1})} \right]. \quad (1)$$

103

104 In this equation, the first term corresponds to the intraband transition, and the
 105 second term corresponds to the direct interband transition. The angular frequency is $\omega =$
 106 $2\pi\nu$, e is the electron charge, \hbar is the reduced Planck constant, and E_f is the doped
 107 graphene Fermi energy. The relaxation time $\tau = \mu E_f / e v_f^2$, where $v_f = c/300$ is the Fermi
 108 velocity and $\mu = 10\,000$ cm² V⁻¹ s⁻¹ is the carrier mobility of graphene.

109 **Generating higher order Fano resonance modes**

110 Here, we take an SRR structure with outer radius $R = 120$ nm, gap $G = 20$ nm,
 111 width $W = 30$ nm and periodic lattice parameter $P = 300$ nm as an example to illustrate
 112 the as-proposed higher order Fano resonance in the mid-infrared range. This dimension
 113 can ensure the excitation energies lower than the energy of graphene's intrinsic optical
 114 phonons (a type of lattice vibration) at 1580 cm⁻¹. Thus the graphene SRR is far away
 115 from the Landau damping region and has a low damping rate.^{15,34} The transmission
 116 spectrum of the SRR exhibits six absorption peaks at 467, 550, 756, 964, 1146 and 1309
 117 cm⁻¹ in the range studied (black curve in Fig. 2a). The calculated method of the
 118 transmission spectrum is described in the ESI.† The SRR structure derives from the
 119 break of symmetry of a graphene ring with a 20 nm gap. For comparison, the
 120 transmission spectrum of the corresponding graphene ring without a slit is also plotted
 121 (red curve in Fig. 2a). The spectrum has only one peak, which is at 467 cm⁻¹. To

122 understand the transmission spectra, the z -complement electric near field of the ring
 123 and SRR at corresponding resonant frequencies are displayed in Fig. 2b. The
 124 electromagnetic field distribution indicates a dipolar oscillation mode in the ring.
 125 However, due to the broken symmetry,³⁵⁻³⁷ there are 4, 6, 8, 10, and 12 nodes in the
 126 electromagnetic field distribution of the SRR, corresponding to Q, O, H, T, and HC dark
 127 modes, respectively.^{37,38} The relation between the node number, m , and the order
 128 number of the mode, n , is $m = 2n$. Thus, the 2^n order electromagnetic resonance is
 129 produced.

130 The radius of the graphene disk r is then designed to overlap with the higher order
 131 plasmon frequency of the SRR in the following. The as-excited plasmons in the
 132 graphene disks are the dipolar electromagnetic resonances, as demonstrated by the
 133 calculated electric near field distribution in Fig. 2d(1). Their plasmon frequency varies
 134 with the disk radius r according to the equation:³⁹⁻⁴²

$$\omega_{\text{pl}} = \sqrt{\frac{e^2 E_f q}{2\pi \hbar^2 \epsilon_0 \epsilon_r}} \propto \sqrt{\frac{E_f}{r \epsilon_r}} \quad (2)$$

135

136 where $q = \pi/2r$ is the wave vector and ϵ_r is determined by the dielectric
 137 environment. Thus, the disk size can be manipulated to adjust the plasmon frequency
 138 to match a higher order resonance mode in the SRR. As shown in Fig. 2c, the
 139 transmission spectra of graphene disks with radii of 60, 43.5 and 34 nm have resonance
 140 frequencies at 979, 1163 and 1323 cm^{-1} , respectively, which correspond to the H, T,
 141 and HC modes of the graphene SRR, respectively.

142 Higher order Fano resonances are generated by inserting a disk into the SRR. The
 143 higher order Fano resonance, i.e. the H, T, and HC Fano modes, occurs when the dipolar
 144 plasmon frequency covers the corresponding higher order mode of the SRR (Fig. 2c).
 145 The dipolar mode in the disk is the bright mode (large resonance peak), while the higher
 146 order SRR modes are dark (small peaks). This is consistent with the near electric field
 147 distributions of the SRR (i.e. weak Q-HC modes in Fig. 2b) and the disk (strong mode

148 in Fig. 2d). Here, the closest separation g between the disk and the gap is chosen as 5
149 nm,⁴³ but when g increases to 15 nm, these modes can still interact with each other well
150 to form the higher order Fano modes (details can be found in the Fig. S2 in the ESI+).
151 To study the physical mechanism of the higher order Fano resonance, the near field
152 distribution in the SRR-disk hybrid structure is analyzed. Take the HC mode as an
153 example. Its near field distribution at two resonance peaks and the transparency window
154 (points 2, 3, and 6 in Fig. 2c) are displayed in Fig. 2d. At point 6, where the strongest
155 destructive coupling happens, the electromagnetic energy of the disk almost completely
156 transfers to the SRR, whose near electric field enhancement is one order of magnitude
157 larger than the SRR alone (Fig. 2b). At points 2 and 3, most of the electromagnetic energy
158 remains in the disk, and the near field strength of the SRR is almost equivalent to that
159 in an individual SRR, indicating a weak-coupling strength between the disk and the
160 SRR. The near field distribution of the H and T Fano modes at the strongest coupling
161 points (points 4 and 5), shown in Fig. 2d, also demonstrate a strong energy transfer
162 between the SRR and the disk.

163 **Refractive-index sensing performance of the higher order Fano** 164 **resonance**

165 We now proceed to evaluate the performance of these separate higher order Fano
166 modes. An 8 nm thick film with different refractive indices is applied over the device
167 as an analyte. Fig. 3a shows the transmission spectra of the HC Fano resonance modes
168 with several typical analytes, *i.e.*, $n = 1$ (air), $n \approx 1.32$ (ethanol), $n \approx 1.41$ (ethylene
169 glycol), and $n \approx 1.56$ (bromoform). Here, the E_f is fixed at 0.5 eV. The transparency
170 window frequency shifts to red (from 1314 cm^{-1} to 1152 cm^{-1}) as the refractive index
171 of the analytes increase from 1 to 1.56. The transparency window frequencies of the H,
172 T, and HC Fano modes are plotted together as a function of the refractive index (Fig.
173 3b). There is a linear change in these frequency shifts, and the slopes of these lines are
174 defined as sensitivities (approximately 195, 239, and 289 cm^{-1} per RIU for the H, T,
175 and HC Fano modes, respectively). This clearly reflects that the sensitivity of the sensor
176 is enhanced by the graphene higher order Fano resonance.

177 The ratio of the sensitivity to the bandwidth of the resonance [(cm⁻¹ per
178 RIU)/bandwidth] determines the FOM of metamaterials. The bandwidth is the full
179 width at half-maximum (FWHM) in the symmetric Fano resonance. In the asymmetric
180 Fano resonance, the bandwidth is the line width from the peak to the dip of the
181 resonance.⁹ The FOM values of the H, T, and HC Fano are around 15, 24, and 29,
182 respectively. It not only reveals that the FOM is on the rise when increasing the order
183 number n of the Fano resonance, but also indicates that the maximum FOM in our
184 structures comes from the HC Fano. To understand this result, the wave vector k_{spp} of
185 the higher order plasmon modes in the SRR satisfy the equations $k_{\text{spp}} \propto n/L$ ⁴⁴⁻
186 ⁴⁷ and $k_{\text{spp}} = \hbar\omega_r^2/(2\alpha_0 E_{\text{FC}})$,^{48,49} where n is the order of the mode, L is the length of the
187 SRR, and $\alpha_0 = e^2/\hbar c$ is the fine-structure constant. Thus, the frequency of the
188 transparency windows in the higher order Fano satisfy the
189 equation $\omega_r \propto \sqrt{nE_{\text{F}}/L} \propto \sqrt{1/(L/n)}$, where L/n is regarded as the effective resonance
190 length of the graphene dipolar plasmon. When the order number n of the Fano
191 resonance is larger, the effective resonance length is shorter. Thus, the frequency shift
192 is faster, and the sensitivity is improved. In addition, the higher order Fano resonance
193 has the narrower FWHM, which decreases from 13 to 9.9 cm⁻¹ corresponding to the
194 range from H to HC Fano resonance. Hence, the sensitivity and FOM are enhanced
195 with the increasing order number n of the Fano resonance.

196 **Dynamic tunability and the SEIRA applications of the higher order**

197 **Fano resonance modes**

198 The ability to tune graphene higher order Fano resonances stemming from its
199 tunable Fermi level is significant for dynamic biosensors. For example, the
200 transparency windows in the transmission spectra of the HC mode increase in resonant
201 strength and shift to blue as E_{F} is adjusted from 0.4 to 0.6 eV (Fig. 4a), which can be
202 realized by chemical doping *via* nitric acid vapor or NO₂.^{15,50} This phenomenon can be
203 interpreted in the following. The resonant frequency of the SRR increases
204 with E_{F} *via* $\omega_r \propto \sqrt{nE_{\text{F}}/L}$. And the graphene disk plasmon frequency also increases

205 with E_f (eqn (2)). Thus, the resulting higher order Fano resonant frequencies can be
 206 tuned by changing the E_f while fixing the structure parameter. We plot the resonant
 207 frequency shifts of the transparency window of the H, T, and HC Fano modes as a
 208 function of $E_f^{1/2}$ in Fig. 4b. The higher order the mode is, then the faster the frequency
 209 shift. Thus, the sensitivity is expressed by the equation $\partial\omega_i / \partial E_f \propto \sqrt{n/L} E_f^{-1/2}$.
 210 When E_f is fixed, a larger n results in greater sensitivity.

211 The dynamical tunable graphene plasmon higher order Fano resonance with a high
 212 electromagnetic field confinement in the mid-infrared range supplies a very promising
 213 route to identify molecules *via* SEIRA. SEIRA is complementary to refractive index
 214 sensors since it can detect molecular vibrational fingerprints. The Fano resonance
 215 exhibits multiple resonant absorption peaks which can reduce the detuning between the
 216 plasmon resonant frequency and multiple vibrational frequencies and can be used as a
 217 platform for enhancing the multiple vibrational modes of molecules. The HC Fano
 218 mode of the asymmetric structure and the dipolar mode of the disk are comparatively
 219 studied for SEIRA application. An 8 nm-thick *tert*-butylamine ((CH₃)₃CNH₂) layer is
 220 used as the analyte which has two vibrational modes at ~ 1220 cm⁻¹ (A) and ~ 1245
 221 cm⁻¹ (B) corresponding to the C–C–C symmetric and anti-symmetric stretches,
 222 respectively. An analytical model based on summing Lorentz oscillators^{51–53} is used to
 223 simulate the molecule's vibrational spectrum (Fig. 5a) as follows:

$$\varepsilon(\omega) = 1 + \sum_{n=1}^N \frac{f_n}{\omega_n^2 - \omega^2 - i\gamma_n\omega} \quad (3)$$

224
 225 where f_n , ω_n and γ_n are parameters characterizing individual
 226 vibrations, *i.e.* ($f_1 = f_2 = 215$ cm⁻², $\gamma_1 = \gamma_2 = 50$ cm⁻¹, $\omega_1 = 1220$ cm⁻¹, $\omega_2 = 1245$ cm⁻¹).
 227 The direct IR absorption of the 8 nm-thick *tert*-butylamine layer is very weak (0.014%)
 228 at A and B, which is undetectable in the commercial FTIR.¹⁸ The graphene E_f is
 229 adjusted to 0.437 eV to realize the spectral overlap between the molecules and graphene
 230 metamaterials. After the enhancement of the graphene metamaterials, the A and B
 231 modes are present as obvious dips in the plasmon resonant absorption spectra (solid

232 lines). As shown, the HC Fano mode has two prominent resonance peaks exactly at the
233 molecular modes (green dashed line) and significantly enhances the signals of both A
234 and B modes. As a comparison, the dipolar plasmon mode (supported graphene disk)
235 only has one resonance peak (orange dashed line). The A vibrational frequency is out
236 of range for the plasmon resonant frequency and the enhanced vibrational signal is
237 much weaker than the B vibrational mode.

238 The difference between absorption spectra, *i.e.* the delta absorption, before and
239 after coating with the *tert*-butylamine film are extracted to calculate the enhancement
240 of IR signals of the vibrational modes. The delta absorptions of the HC modes are
241 displayed in Fig. 5b. The enhancement factors of both the A and B modes are up to 425-
242 fold from the HC order Fano modes. However, the enhancement factor of the A mode
243 is only 75, about 7.5 times smaller than that of the B mode (enhanced 554-fold).

244

245 **Conclusions**

246 In summary, pure high-quality, higher order Fano resonances have been demonstrated
247 in graphene plasmonic metamaterials. The crosstalk between different higher order
248 Fano modes is avoided due to the narrow bandwidth of the graphene plasmon resulted
249 from its low damping. The higher order Fano modes have superior refractive-index
250 sensing performances because the spectral shifts induced by the analyte increase with
251 the Fano mode order. In this work, the frequency sensitivity and FOM of the HC mode
252 are able to reach 289 cm^{-1} per RIU and 29, respectively, for an 8 nm thick analyte.
253 Moreover, these graphene Fano modes can also be tuned to probe the infrared
254 vibrational fingerprints of the analyte with a significant signal enhancement (>400
255 times). Therefore, our proposed higher order Fano structures are a promising device for
256 nanoscale optical sensing.

257

258 **Conflicts of interest**

259 There are no conflicts to declare

260

261 **Acknowledgements**

262 This work was supported by The National Basic Research Program of China (Grant No.
263 2015CB932400, 2016YFA0201600), the National Natural Science Foundation of
264 China (Grant No. 51372045, 11504063, 11674073), the Bureau of International
265 Cooperation, Chinese Academy of Sciences (121D11KYSB20130013), and the Key
266 Program of the Bureau of Frontier Sciences and Education Chinese Academy of
267 Sciences (QYZDB-SSW-SLH021)

268

269 **References**

270 1 B. Luk'yanchuk, N. I. Zheludev, S. A. Maier, N. J. Halas, P. Nordlander, H. Giessen and C. T. Chong,
271 *Nat. Mater.*, 2010, 9, 707–715.

272 2 C. Wu, A. B. Khanikaev, R. Adato, N. Arju, A. A. Yanik, H. Altug and G. Shvets, *Nat. Mater.*, 2011, 11,
273 69–75.

274 3 N. Verellen, Y. Sonnefraud, H. Sobhani, F. Hao, V. V. Moshchalkov, P. V. Dorpe, P. Nordlander and S.
275 A. Maier, *Nano Lett.*, 2009, 9, 1663–1667.

276 4 Y. Zhang, T. Li, B. Zeng, H. Zhang, H. Lv, X. Huang, W. Zhang and A. K. Azad, *Nanoscale*, 2015, 7,
277 12682–12688.

278 5 N. Liu, T. Weiss, M. Mesch, L. Langguth, U. Eigenthaler, M. Hirscher, C. Sonnichsen and H. Giessen,
279 *Nano Lett.*, 2010, 10, 1103–1107.

280 6 W. Tang, L. Wang, X. Chen, C. Liu, A. Yu and W. Lu, *Nanoscale*, 2016, 8, 15196–15204.

281 7 F. Hao, P. Nordlander, Y. Sonnefraud, P. V. Dorpe and S. A. Maier, *ACS Nano*, 2009, 3, 643–652.

282 8 M. Amin, M. Farhat and H. Bagci, *Sci. Rep.*, 2013, 3, 2105.

283 9 Y. H. Fu, J. B. Zhang, Y. F. Yu and B. Luk'yanchuk, *ACS Nano*, 2012, 6, 5130–5137.

284 10 Y. Sonnefraud, N. Verellen, H. Sobhani, G. A. Vandenbosch, V. V. Moshchalkov, P. Van Dorpe, P.
285 Nordlander and S. A. Maier, *ACS Nano*, 2010, 4, 1664–1670.

286 11 Q. Zhang, X. Wen, G. Li, Q. Ruan, J. Wang and Q. Xiong, *ACS Nano*, 2013, 7, 11071–11078.

287 12 N. Verellen, P. Van Dorpe, C. Huang, K. Lodewijks, G. A. Vandenbosch, L. Lagae and V. V.
288 Moshchalkov, *Nano Lett.*, 2011, 11, 391–397.

289 13 H. Liu, Z. Wang, J. Huang, Y. J. Liu, H. J. Fan, N. I. Zheludev and C. Soci, *Nano Lett.*, 2014, 14,

290 5162– 5169.

291 14 Y. Zhang, T. Jia, H. Zhang and Z. Xu, *Opt. Lett.*, 2012, 37, 4919–4921.

292 15 H. Yan, T. Low, W. Zhu, Y. Wu, M. Freitag, X. Li, F. Guinea, P. Avouris and F. Xia, *Nat. Photonics*,

293 2013, 7, 394–399.

294 16 X. Yang, F. Zhai, H. Hu, D. Hu, R. Liu, S. Zhang, M. Sun, Z. Sun, J. Chen and Q. Dai, *Adv. Mater.*,

295 2016, 28, 2931– 2938.

296 17 J. Christensen, A. Manjavacas, S. Thongrattanasiri, F. H. Koppens and F. J. García de Abajo, *ACS*

297 *Nano*, 2011, 6, 431–440.

298 18 H. Hu, X. Yang, F. Zhai, D. Hu, R. Liu, K. Liu, Z. Sun and Q. Dai, *Nat. Commun.*, 2016, 7, 12334.

299 19 D. Rodrigo, O. Limaj, D. Janner, D. Etezadi, F. J. G. de Abajo, V. Pruneri and H. Altug, *Science*, 2015,

300 349, 165–168.

301 20 R. Adato, A. A. Yanik, J. J. Amsden, D. L. Kaplan, F. G. Omenetto, M. K. Hong, S. Erramilli and H.

302 Altug, *Proc. Natl. Acad. Sci. U. S. A.*, 2009, 106, 19227– 19232.

303 21 I. M. Pryce, Y. A. Kelaita, K. Aydin and H. A. Atwater, *ACS Nano*, 2011, 5, 8167–8174.

304 22 N. Liu, L. Langguth, T. Weiss, J. Kastel, M. Fleischhauer, T. Pfau and H. Giessen, *Nat. Mater.*, 2009,

305 8, 758–762.

306 23 S. Zhang, D. A. Genov, Y. Wang, M. Liu and X. Zhang, *Phys. Rev. Lett.*, 2008, 101, 047401.

307 24 X. Zhao, C. Yuan, L. Zhu and J. Yao, *Nanoscale*, 2016, 8, 15273–15280.

308 25 V. W. Brar, M. S. Jang, M. Sherrott, J. J. Lopez and H. A. Atwater, *Nano Lett.*, 2013, 13, 2541–2547.

309 26 M. Abb, Y. Wang, N. Papasimakis, C. De Groot and O. L. Muskens, *Nano Lett.*, 2013, 14, 346–352.

310 27 M. Abb, Y. Wang, N. Papasimakis, C. H. de Groot and O. L. Muskens, *Nano Lett.*, 2014, 14, 346–

311 352.

312 28 X. T. Kong, X. Yang, Z. Li, Q. Dai and X. Qiu, *Opt. Lett.*, 2014, 39, 1345–1348.

313 29 E. D. Palik, *Handbook of optical constants of solids*, Academic Press, London, 1985.

314 30 P.-Y. Chen and A. Alù, *ACS Nano*, 2011, 5, 5855–5863.

315 31 L. A. Falkovsky and S. S. Pershoguba, *Phys. Rev. B: Condens. Matter*, 2007, 76, 153410.

316 32 B. Vasić, M. M. Jakovljević, G. Isić and R. Gajić, *Appl. Phys. Lett.*, 2013, 103, 011102.

317 33 V. P. Gusynin, S. G. Sharapov and J. P. Carbotte, *J. Phys.: Condens. Matter*, 2007, 19, 026222.

318 34 H. Buljan, M. Jablan and M. Soljačić, *Nat. Photonics*, 2013, 7, 346–348.

319 35 F. Hao, E. M. Larsson, T. A. Ali, D. S. Sutherland and P. Nordlander, *Chem. Phys. Lett.*, 2008, 458,

320 262–266.

321 36 H. Wang, Y. Wu, B. Lassiter, C. L. Nehl, J. H. Hafner, P. Nordlander and N. J. Halas, Proc. Natl. Acad.
322 Sci. U. S. A., 2006, 103, 10856–10860.

323 37 A. K. Sheridan, A. W. Clark, A. Glidle, J. M. Cooper and D. R. S. Cumming, Appl. Phys. Lett., 2007,
324 90, 143105.

325 38 C. Rockstuhl, F. Lederer, C. Etrich, T. Zentgraf, J. Kuhl and H. Giessen, Opt. Express, 2006, 14, 8827–
326 8836.

327 39 H. Hu, F. Zhai, D. Hu, Z. Li, B. Bai, X. Yang and Q. Dai, Nanoscale, 2015, 7, 19493–19500.

328 40 S. H. Abedinpour, G. Vignale, A. Principi, M. Polini, W.-K. Tse and A. H. MacDonald, Phys. Rev. B:
329 Condens. Matter, 2011, 84, 045429.

330 41 A. N. Grigorenko, M. Polini and K. S. Novoselov, Nat. Photonics, 2012, 6, 749–758.

331 42 R. Liu, B. Liao, X. Guo, D. Hu, H. Hu, L. Du, H. Yu, G. Zhang, X. Yang and Q. Dai, Nanoscale, 2017,
332 9, 208–215.

333 43 X.-j. Shang, X. Zhai, X.-f. Li, L.-l. Wang, B.-x. Wang and G.-d. Liu, Plasmonics, 2016, 11, 419–423.

334 44 X. Shi, D. Han, Y. Dai, Z. Yu, Y. Sun, H. Chen, X. Liu and J. Zi, Opt. Express, 2013, 21, 28438–
335 28443.

336 45 S. Liu, Z. Zhang and Q. Wang, Opt. Express, 2009, 17, 2906–2917.

337 46 P. Nordlander, ACS Nano, 2009, 3, 488–492.

338 47 P. Liu, W. Cai, L. Wang, X. Zhang and J. Xu, Appl. Phys. Lett., 2012, 100, 153111.

339 48 H. Cheng, S. Chen, P. Yu, X. Duan, B. Xie and J. Tian, Appl. Phys. Lett., 2013, 103, 203112.

340 49 F. H. Koppens, D. E. Chang and F. J. Garcia de Abajo, Nano Lett., 2011, 11, 3370–3377.

341 50 A. L. Falk, K. C. Chiu, D. B. Farmer, Q. Cao, J. Tersoff, Y. H. Lee, P. Avouris and S. J. Han, Phys.
342 Rev. Lett., 2017, 118, 257401.

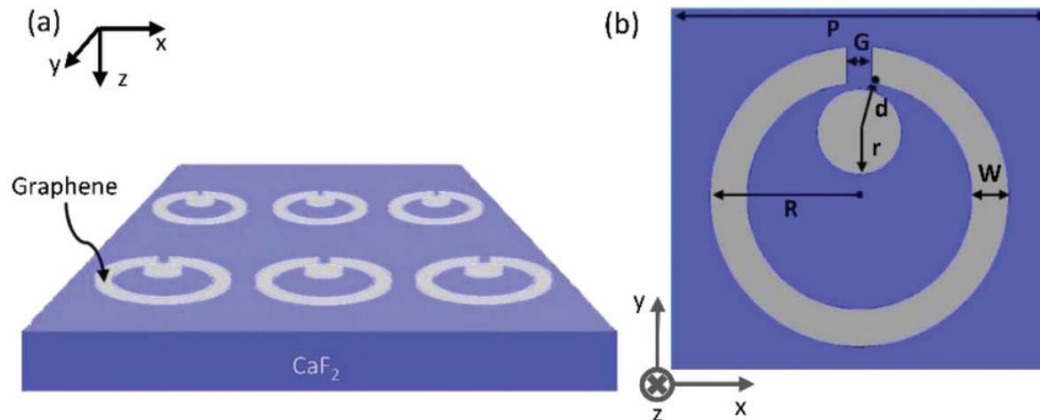
343 51 F. Liu and E. Cubukcu, Phys. Rev. B: Condens. Matter, 2013, 88, 115439.

344 52 A. Marini, I. Silveiro and F. J. García de Abajo, ACS Photonics, 2015, 2, 876–882.

345 53 E. Cubukcu, S. Zhang, Y.-S. Park, G. Bartal and X. Zhang, Appl. Phys. Lett., 2009, 95, 043113.

346

347

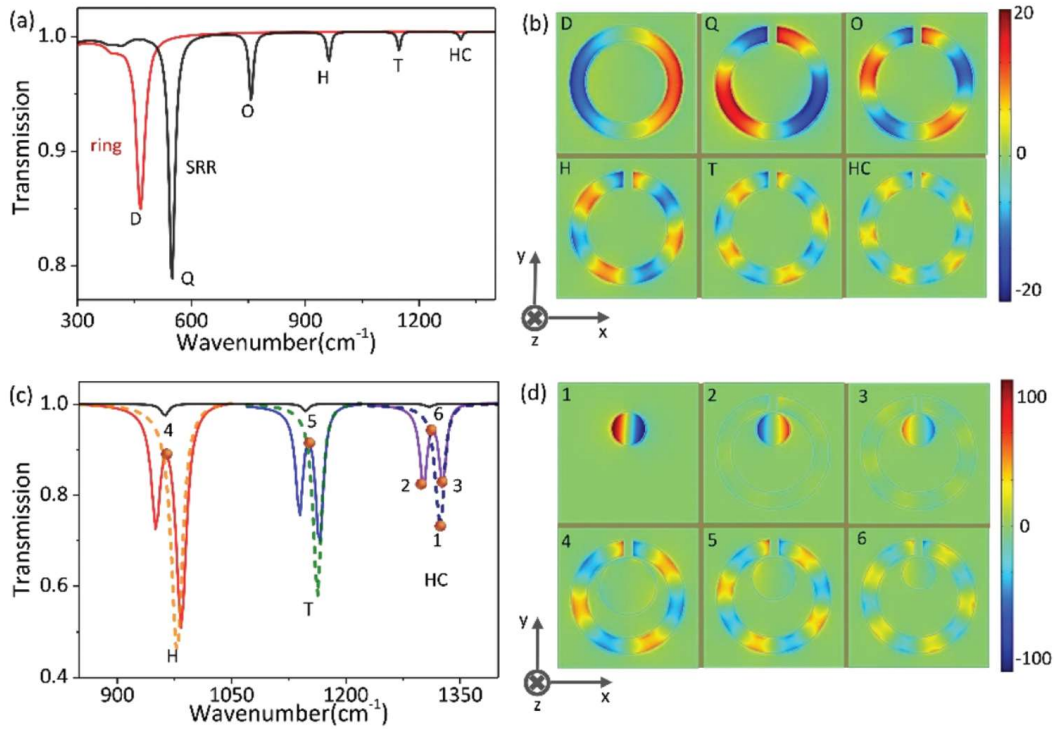


348

349 **Fig. 1** (a) Schematic of the graphene metamaterial comprised of a disk and an SRR in
350 a unit cell. (b) Top view of a unit cell: fixed periodicity $P = 300$ nm, outer radius $R =$
351 120 nm, width $W = 30$ nm, and gap $G = 20$ nm of the graphene SRR, and the closest
352 separation distance $g = d - r$ of the graphene disk and SRR.

353

354



355

356 **Fig. 2** (a) Transmission spectra of the ring array (red) and SRR array (black). (b)

357 Electric near field distributions (the z -complement, normalized to the incident light) of

358 the ring and SRR unit cell of different modes. (c) The transmission spectra of the Fano

359 metamaterials with H, T, and HC order modes (colored solid lines), respectively. The

360 transmission spectra of the individual disk array (dashed lines) and SRR array (black)

361 are also plotted. (d) Normalized z -complement electric near field distributions of

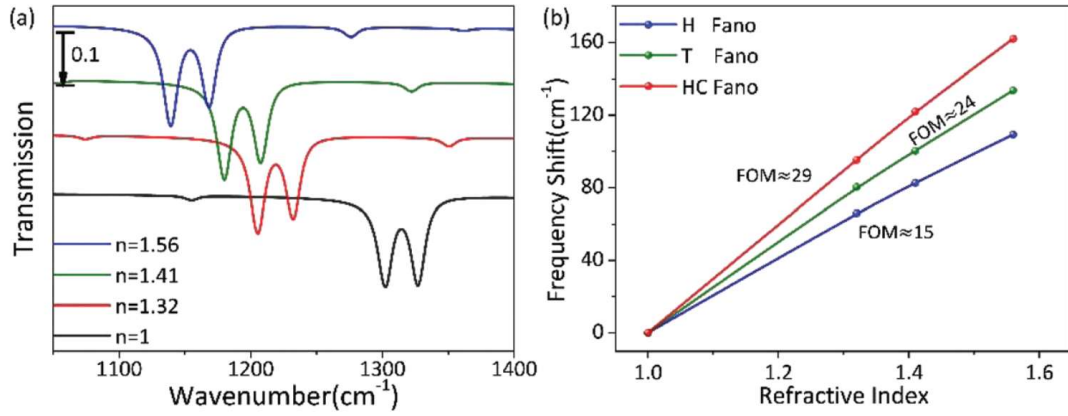
362 different modes at frequencies: (1) 1323 cm^{-1} , (2) 1304 cm^{-1} , (3) 1327 cm^{-1} , (4) 963

363 cm^{-1} , (5) 1150 cm^{-1} and (6) 1314 cm^{-1} , as marked with orange dots in (c). The cutting

364 plane is 2 nm above the bottom of the graphene metamaterials. The graphene E_f is 0.5

365 eV.

366

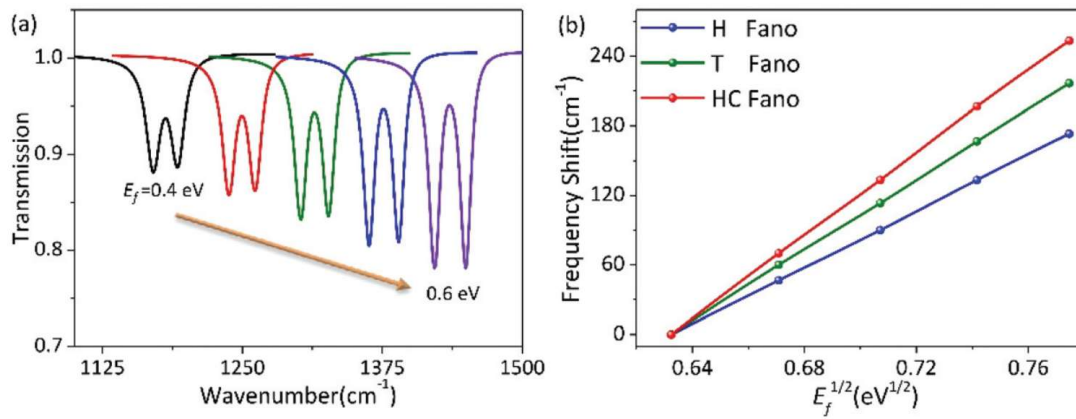


367

368 **Fig. 3** (a) Simulated transmission spectra of the HC Fano resonance mode with different
 369 analytes (marked by refractive indices). (b) Frequency shift of H, T, and HC Fano
 370 resonance modes *versus* the refractive index of the analyte. The corresponding FOM
 371 values are also shown.

372

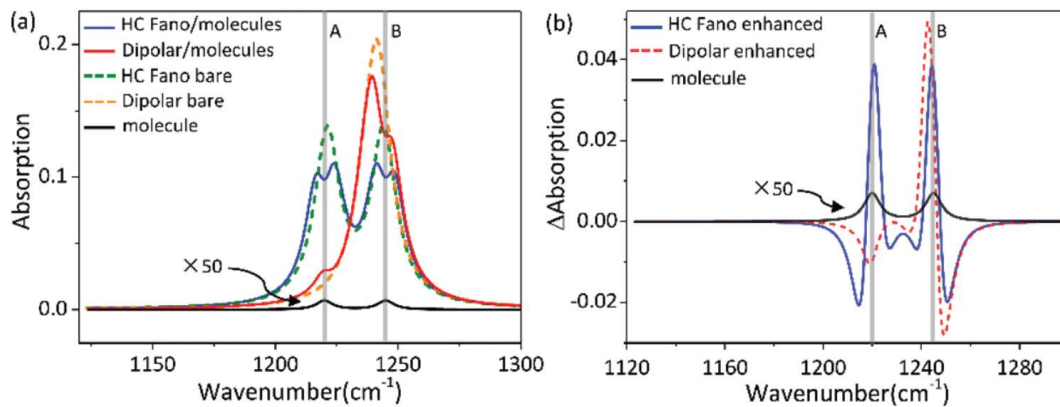
373



374

375 **Fig. 4** (a) Simulated transmission spectra of the HC Fano resonance structure
376 with E_f varied from 0.4 eV to 0.6 eV. (b) The peak frequency in the transparency
377 window of H, T, and HC Fano resonance modes in the transmission spectra as a function
378 of $E_f^{1/2}$

379



380

381 **Fig. 5** (a) Absorption spectra of graphene HC Fano modes and the corresponding
 382 graphene disk before (dashed lines) and after (solid lines) the analyte layer coating with
 383 an E_f of 0.437 eV. The absorption spectrum of the 8 nm-thick *tert*-butylamine is also
 384 plotted (black curve), with two vibrational modes A and B. (b) The molecular
 385 vibrational mode response in plasmon resonant peaks extracted from (a).

386

Supplementary Information

Higher order Fano graphene metamaterials for nanoscale optical sensing

Xiangdong Guo,^{a,b,c} Hai Hu,^{a,c} Xing Zhu,^{a,b,d} Xiaoxia Yang,^{*a} Qing Dai^{*a}

^a China CAS Center for Excellence in Nanoscience, National Center for Nanoscience and Technology, Beijing 100190, P. R. China

^b Academy for Advanced Interdisciplinary Studies, Peking University, Beijing 100871, P. R. China

^c University of Chinese Academy of Sciences, Beijing 100049, P. R. China

^d State Key Lab for Mesoscopic Physics, School of Physics, Peking University, Beijing 100871, P. R. China.

†Corresponding E-mail: daiq@nanoctr.cn, yangxx@nanoctr.cn

Simulation method for transmission spectra

Considering the 3D FEM calculated amount and the mesh quality, the smallest mesh size of graphene is 0.5 nm and the mesh size gradually increases outside the graphene layer, which can reach proper convergence. In addition, the graphene layer is ultra-thin, which is treated as the inner boundary conditions (transition boundary condition) with the thickness 1 nm in our simulation.

In the the simulation, the periodicity of the metamaterials ($P = 300$ nm) is much less than the resonance wavelength (around $7\sim 10$ μm), thus there isn't the high order diffraction. Hence the transmission (T) data is extracted from the S_{21} parameter:¹

$$T = |S_{21}|^2$$

The definition of the S-parameters in terms of the power flow is:

$$S_{21} = \sqrt{\frac{\text{Power delivered to port 2}}{\text{Power incident on port 1}}}$$

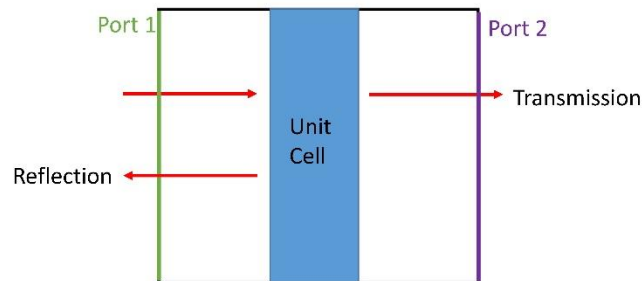


Fig. S1 Schematic illustration of the transmission data is extracted by the FEM simulation.

The effect of the closest separation in SRR/disk

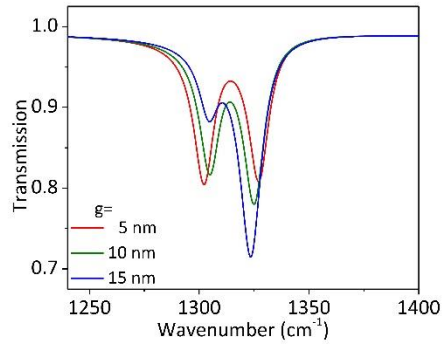


Fig. S2 Transmission spectra of the HC Fano resonance structure with the closest gap varied from 5 to 15 nm, and the Fermi energy is 0.5 eV.

The Fano resonance is still obvious when the nanogap is below 15 nm in our structure as demonstrated in Fig. S2. With the nanogap increasing from 5 to 15 nm, the coupling efficiency of the Fano resonance would decrease, but the pure higher order graphene Fano resonance is still created to avoid the crosstalk in refractive-index sensing. Thus, the closest gap can be selected more than 5 nm in the experiment. In addition, with the rapid development of nanofabrication technologies such as focused ion beam (FIB) and electron beam lithography (EBL), the accuracy of nanogap would become higher. The smallest nanogap has been realized around 1.5~10 nm by FIB² and 4 nm by EBL³. Hence we think it is possible to fabricate the metamaterials with the rapid development of nanofabrication technologies.

Notes and references

1. J. S. Gomez-Diaz and J. Perruisseau-Carrier, *Opt Express*, 2013, 21, 15490-15504.
2. M. D. Fischbein and M. Drndić, *Nano letters*, 2007, 7, 1329-1337.
3. Y. Sonnefraud, N. Verellen, H. Sobhani, G. A. Vandenbosch, V. V. Moshchalkov, P. Van Dorpe, P. Nordlander and S. A. Maier, *ACS nano*, 2010, 4, 1664-1670.